Applied Surface Science 534 (2020) 147608

Contents lists available at ScienceDirect

Applied Surface Science

journal homepage: www.elsevier.com/locate/apsusc

Organic pillars pre-intercalated V^{4+}-$V_2O_5{\cdot}3H_2O$ nanocomposites with enlarged interlayer and mixed valence for aqueous Zn-ion storage

Honglin Yan[a], Qiang Ru[a,*], Ping Gao[a], Zhenglu Shi[a], Yuqing Gao[a], Fuming Chen[a], Francis Chi-Chun Ling[b], Li Wei[c]

[a] Guangdong Engineering Technology Research Center of Efficient Green Energy and Environmental Protection Materials, Guangdong Provincial Key Laboratory of Quantum Engineering and Quantum Materials, School of Physics and Telecommunication Engineering, South China Normal University, Guangzhou 510006, China
[b] Department of Physics, The University of Hong Kong, Pokfulam Road, Hong Kong, China
[c] School of Chemical and Biomolecular Engineering, The University of Sydney, Australia

ARTICLE INFO

Keywords:
Aqueous Zn-ion batteries
Organic PAN/THF pillars
Mixed V4+/V5+ valence
In-XRD

ABSTRACT

As cathodes for aqueous Zn-ion batteries, the repetitive insertion/extraction and strong polarization of Zn^{2+} during cycles will severely wreck the structure of layered vanadium oxides, resulting in rapid capacity recession. Hence, the ingenious strategy of PAN/THF-pillars intercalation and V^{4+}/V^{5+} dual-valence regulation was designed to fabricate PAN or THF pre-intercalated V^{4+}-$V_2O_5{\cdot}3H_2O$, denoted as P-VO or T-VO. Owing to the interlayer expansion of organic molecules and the electrochemical reactivity enhancement of mixed V^{4+}/V^{5+} valence, severe structural collapse of cathodes and strong polarization of Zn^{2+} can be alleviated. Hence, P-VO and T-VO cathodes can exhibit larger interlayer distances of 13.67 and 14.41 Å, more robust construction, faster Zn^{2+} transmission, and better electrical conductivity. P-VO and T-VO electrodes furnish high zinc storage performance of 251 and 336 mAh g^{-1} at 500 mA g^{-1}, and persistently maintain considerable reversible capacities of 133 and 100 mAh g^{-1} after 1000 cycles at a high current density of 10 A g^{-1}. And the capacitive contribution ratios of P-VO and T-VO can reach up to 75% and 86.4%, respectively. Meanwhile, both two cathodes can endure extreme ambient conditions from −15 °C to 45 °C. In addition, the insertion mechanism of Zn^{2+} was also investigated via in-situ XRD and ex-situ XPS.

1. Introduction

In the past few years, conventional lithium ion batteries (LIBs) as rechargeable power suppliers have widely occupied the predominant market of portable electronics and automotive vehicles [1,2]. Whereas, owing to the vast application of LIBs, some demerits, such as insufficient lithium resource, latent safety loophole, and undesired environmental pollution, have been exposed [3]. Hence, searching for alternative energy storage systems has been an urgent task for researchers. Nowadays, many aqueous rechargeable batteries are taken into consideration due to intrinsic merits of high security, good ionic conductivity, and environmental benignity [4-6]. Among these, zinc has relatively low redox potential (-0.763 V vs. SHE) and high theoretical capacity (819 mAh g^{-1}) [7]. Therefore, lots of efforts have been devoted to study on aqueous Zn-ion batteries (AZIBs). In addition, both high energy density and superior power density of AZIBs also can be achieved by multiple electrons transfer during electrochemical reaction. Nevertheless, most cathodes of AZIBs still suffer from the drastic structural destruction induced by the adverse features of Zn^{2+} (large hydrated ion radius, high polarization, and strong electrostatic interaction) [8]. Consequently, the application of these cathode materials will be restricted due to inferior cycling life, low specific capacity, and poor rate capability.

Recently, one of the cutting-edge researches in AZIBs is the adoption of vanadium oxides with layered, tunnel structure, and open framework. In 2016, a layered V_2O_5 cathode with a high capacity of 170 mAh g^{-1} for AZIBs was reported by Johnson [9]. Nevertheless, repetitive Zn^{2+}-intercalation/extraction often destroys the host framework and causes rapid capacity degradation [10]. In addition, the sluggish Zn^{2+} insertion kinetics will result in the accumulation of Zn^{2+} in lattice, forming undesired irreversible phases [8]. The availability of metal ion pre-intercalated V_2O_5 host materials for enhancing Zn^{2+} storage capability has been conducted, such as $Li_xV_2O_5{\cdot}nH_2O$, $Ca_{0.25}V_2O_5{\cdot}nH_2O$, $K_{0.25}V_2O_5$, $Na_{0.33}V_2O_5$, $Ag_{0.4}V_2O_5$ and $Mg_xV_2O_5$ [11-16]. However, it will be more difficult to choose other suitable metal ions, owing to the limited select range of metal element. In the past years, via adjustable

* Corresponding author.
E-mail address: rq7702@yeah.net (Q. Ru).

https://doi.org/10.1016/j.apsusc.2020.147608
Received 18 June 2020; Received in revised form 14 August 2020; Accepted 15 August 2020
Available online 18 August 2020

intercalation of organic molecules, 2D $VOPO_4$ nanosheets and MnO_2 nanolayers show much expansile interlayers, which can enhance the cycling stability, rate capability, and ion transport kinetics, significantly [17-19]. Additionally, it is proved that mixed V^{4+}/V^{5+} in V_2O_5 is beneficial to achieving higher electrochemical reactivity, faster ion diffusion, lower polarization, and higher electrical conductivity. For example, Liang's group reported that V_2O_5 with mixed valence exhibits prominent long-term cycling performance, and remains a reversible capacity of 140 mAh g^{-1} after 1000 cycles at 10 A g^{-1} [20].

Therefore, we designed an integrated modification strategy of organic pillars expansion and V^{4+}/V^{5+} dual-valence regulation to boost Zn^{2+} storage capacity and enhance electrochemical reactivity, synchronously. Novel PAN/THF pre-intercalated V^{4+}-$V_2O_5{\cdot}3H_2O$ nanocomposites were fabricated via one-pot hydrothermal method. It is well known that PAN and THF organics are inclined to form hydrogen bond with vanadium oxides. Besides, the N atoms of PAN and O atoms of THF may form donor–acceptor bond with V atoms of $V_2O_5{\cdot}3H_2O$ layers through sharing lone-pair electrons [21]. Hence, the PAN and THF pillars can steadily support the layers of $V_2O_5{\cdot}3H_2O$, which can enlarge the d-spacing of (0 0 1) plane to 13.67 and 14.41 Å, thus accelerating the diffusion of Zn^{2+} (see Schematic 1). Otherwise, the introduction of mixed V^{4+}/V^{5+} valence is also beneficial to accomplishing better electrochemical reactivity of vanadium oxides and relieving the polarization of Zn^{2+} in cathodes.

On account of enlarged interlayer distance, strong support of organic pillars, and electrochemical reactivity enhancement of mixed V^{4+}/V^{5+} valence, PAN pre-intercalated V^{4+}-$V_2O_5{\cdot}3H_2O$ (P-VO) and THF pre-intercalated V^{4+}-$V_2O_5{\cdot}3H_2O$ (T-VO) nanocomposites deliver fast Zn^{2+} diffusion, long cycling performance, and excellent rate capability. Therefore, both P-VO and T-VO cathodes can provide reversible discharge capacities of 251 and 336 mAh g^{-1} at 500 mA g^{-1}. Even the current density increases to 10 A g^{-1}, these cathodes still maintain 133 and 100 mAh g^{-1} after 1000 cycles. And considerable reversible capacities can be furnished at the extreme temperature range of −15 °C to 45 °C. At 500 mA g^{-1}, P-VO and T-VO can exhibit 154 and 125 mAh g^{-1} under −15 °C. When the temperature rises to 45 °C, high discharge capacities of 281 and 273 mAh g^{-1} can be obtained, respectively.

2. Experiment section

2.1. Synthesis of PAN/THF pre-intercalated V^{4+}-$V_2O_5{\cdot}3H_2O$

In a typical procedure, 0.18 g commercial V_2O_5 powder (Energy chemical, 99%) was dispersed in 30 mL deionized water. After stirring for 10 min, 120 μl aniline (Aladdin, 99%) or tetrahydrofuran (Aladdin, 97%) was also added, and the pH was adjusted to 3 using 3 M HCl diluent. After stirring for 30 min, the mixed solution was transferred to 150 mL Teflon vessel in an electric oven at 140 °C for 48 h. After that, the as-prepared samples were washed several times with deionized water and ethanol in sequence, and dried at 80 °C overnight. The final products of PAN/THF pre-intercalated V^{4+}-$V_2O_5{\cdot}3H_2O$ were defined as P-VO and T-VO, respectively.

2.2. Characterization methods

To analyze the morphology of P-VO and T-VO cathodes, Field-emission scanning electron microscope (FESEM) was performed using ZEISS Gemini 500 and Transmission electron microscope (TEM) was carried out on JEM-2100HR. The crystal structure was investigated using X-ray diffraction (XRD; PANalytial X'pert PRO) measurement. Raman spectrum was obtained on inVia. Fourier-transform infrared reflection (FTIR) spectra were recorded on Vertex 70. Additionally, the phase evolutions and valence changes of electrodes at different charging/discharging states were acquired by utilizing in-situ XRD (D8 Venture) and ex-situ X-ray photoelectron spectroscopy (XPS; Escalab 250Xi). The weight loss of composites was obtained by using thermogravimetric analysis (TGA; HQT-4).

2.3. Electrochemical characterization

The working electrodes were composed of P-VO or T-VO powder, conductive carbon black, and poly(vinylidene fluoride) (PVDF) in a weight ratio of 7:2:1. Titanium foils were applied as current collectors. CR2032 coin-type cells in air were assembled by using P-VO or T-VO electrode as cathode, metal zinc as counter electrode, Whatman glass fiber as separator, and 2 M $Zn(CF_3SO_3)_2$ as electrolyte. After that, galvanostatic charge–discharge (GCD) and high-low temperature tests were carried out with a voltage range of 0.4–1.4 V on Land CT2001A.

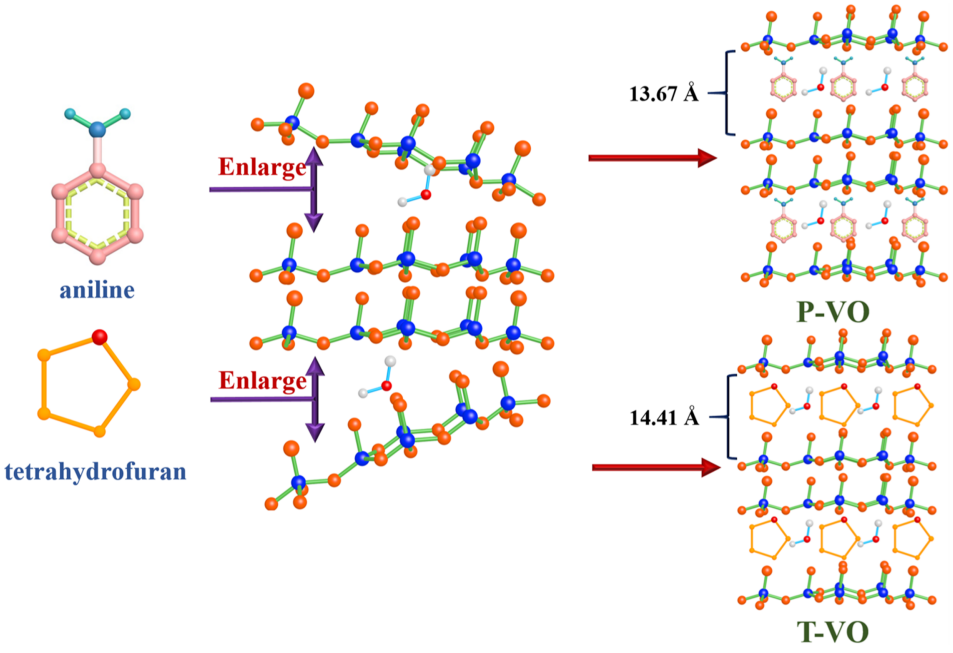

Schematic 1. The illustration of PAN/THF pillars pre-intercalated V^{4+}-$V_2O_5{\cdot}3H_2O$.

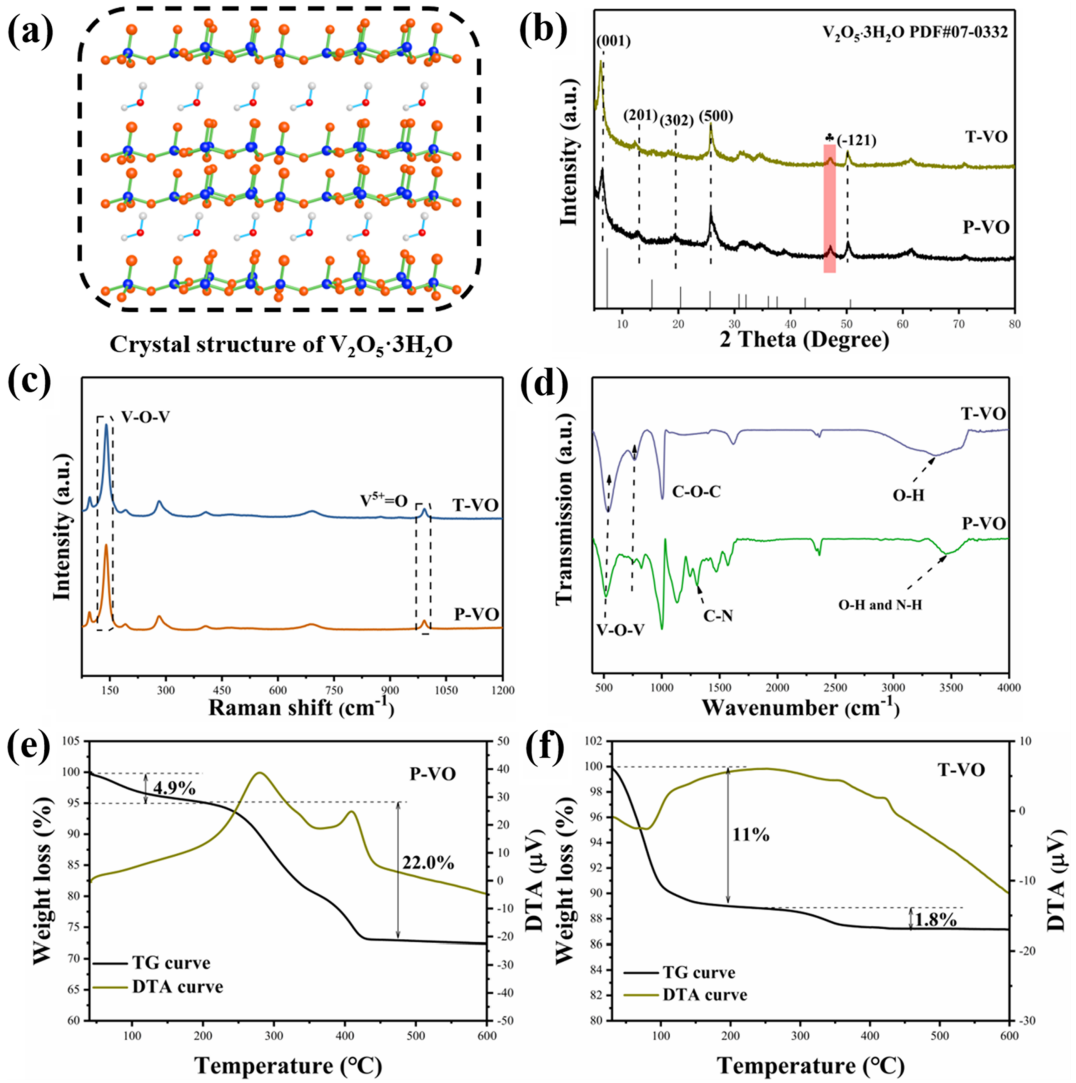

Fig. 1. The crystal structure of $V_2O_5{\cdot}3H_2O$ (a), XRD (b), Raman (c), FTIR spectra (d), and TGA curves (e-f) of P-VO and T-VO.

Cyclic voltammetry (CV) measurements at 0.4–1.4 V and Electrochemical Impedance Spectroscopy (EIS) measurements with the frequency region of 100 kHz–0.01 Hz were conducted on electrochemical workstation (1470E/1400). Galvanostatic Intermittent Titration Technique (GITT) was carried out to estimate the Zn^{2+} diffusion coefficients of P-VO and T-VO, the durations of current pulse and relaxation time are set as 1800 and 3600 s.

3. Result and discussion

3.1. Physical characterization

The $V_2O_5{\cdot}3H_2O$ bilayers are built from multiple VO_5 square pyramid and VO_4 tetrahedra as shown in Fig. 1a, and the interlayers could be adjusted moderately via guest molecules/ions intercalation strategy [22]. In Fig. 1b, both P-VO and T-VO samples present similar characteristic peaks, which are well-consistent with monoclinic $V_2O_5{\cdot}3H_2O$ (PDF#07-0332), and another peak labeled with "♣" is corresponding to $H_xV_2O_5$. It is worth noting that (001), (201), and (302) diffraction peaks of P-VO and T-VO composites shift to lower 2θ degree in comparison to standard $V_2O_5{\cdot}3H_2O$. The left excursion of (001) peaks implies the broadened interlayer spacing, which can be calculated as 13.67 and 14.41 Å, respectively. The enlarged d-spacing is ascribed to the interlayer expansion effect of PAN and THF. Raman spectra of two composites are portrayed in Fig. 1c to indicate the similar characteristic peaks with typical V_2O_5, seven obvious peaks can be observed at 94, 140, 191, 283, 407, 689, and 991 cm^{-1}. The strongest peak located at 140 cm^{-1} is ascribed to the stretching vibration of V-O-V bonds, and the peak at 991 cm^{-1} is attributed to the stretching of V^{5+}=O [14]. Owing to the limited content of PAN and THF in composites, the Raman signals stemmed from PAN and THF may be shielded by the strong Raman peaks of $V_2O_5{\cdot}3H_2O$. Inversely, the existence of PAN and THF can be evidenced by FTIR measurement. As shown in Fig. 1d, the characteristic peaks of C-N and N-H bonds originated from PAN can be found at 1303 and 3470 cm^{-1}, respectively [23]. Meanwhile, the peak of C-O-C bond stemmed from THF can be observed at 1007 cm^{-1}. Additionally, TGA curves of P-VO and T-VO samples are plotted in Fig. 1(e–f), the total weight loss of P-VO and T-VO are 26.9% and 12.8%, which can be ascribed to evaporation of physically adsorbed water, removal of structural water, and decomposition of organic molecules (PAN and THF) [24].

Meanwhile, owing to the reduction effect of hydrothermal process, partial V^{5+} in P-VO and T-VO can be reduced to V^{4+}. In Fig. 2a, the V $2p_{3/2}$ spectrum of pristine P-VO composite can be fitted into a strong peak of V^{5+} at 517.2 eV and a weak peak of V^{4+} at 515. 7 eV [25]. Similarly, T-VO cathode also illustrates two peaks associated with V^{5+} and V^{4+}. Based on the integral area, the V^{5+}/V^{4+} ratios of P-VO and T-VO are calculated to be 4.84:1 and 4.59:1. In addition, the

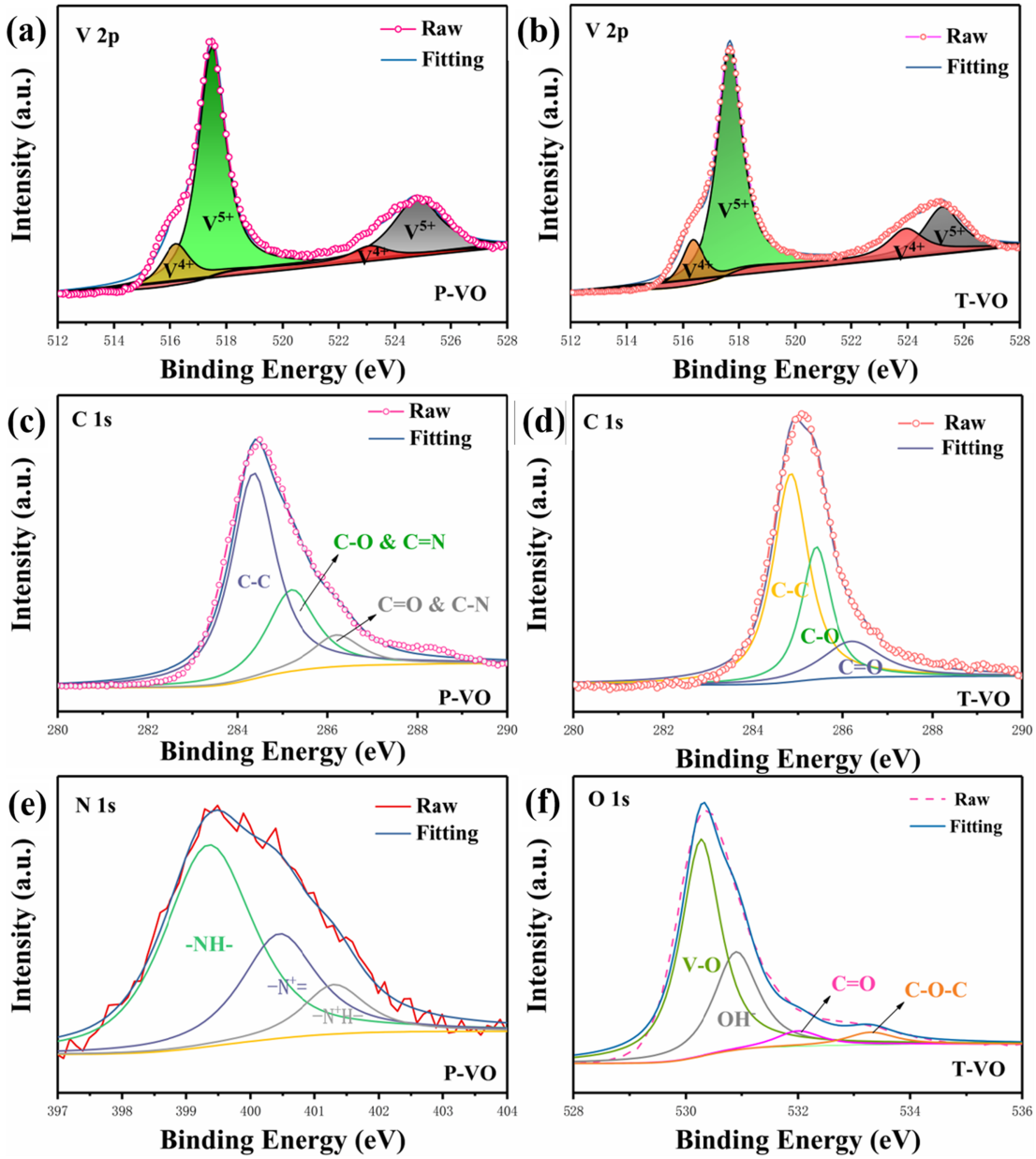

Fig. 2. XPS analysis: V 2p (a), C 1s (c), N 1s (e) of P-VO, and V 2p (b), C 1s (d), O 1s (f) of T-VO.

corresponding XPS signals of PAN and THF also can be detected. As shown in Fig. 2b, the C 1s spectrum of P-VO is composed of three peaks corresponding to C−C (284.4 eV), C−O&C═N (285.2 eV), and C═O& C−N (286.2 eV), of which the C═N and C−N bonds are derived from PAN. The signals of benzenoid amine (−NH−), positively charged nitrogen atoms (−N^+═), and amino nitrogen atoms (−N^+H−) in PAN are also detected at 399.4 eV, 400.5 eV, and 401.3 eV, as shown in Fig. 2e. Meanwhile, C 1s spectrum of T-VO also illustrates three peaks of C−C, C−O, C═O located at 284.8 eV, 285.4 eV, and 286.2 eV, of which the C−O bond is related to THF. And in Fig. 2f, O 1s spectrum shows the C−O−C stemmed from THF is located at 533.3 eV [26]. Other peaks located at 530.3 eV, 530.9 eV, and 532.0 eV are attributed to V−O, OH^-, and C═O, respectively. Hence, the XPS analysis sufficiently proves that the existence of V^{4+}/V^{5+} dual-valence and the insertion of PAN/THF pillars in $V_2O_5{\cdot}3H_2O$.

Morphology and microstructure would influence the specific surface value. As shown in Fig. 3, T-VO nanobelts show the interlaced dispersion, this construction owns more open spaces and is expected to have higher specific surface. As comparison, crisscrossed leaf-like P-VO nanosheets with smooth surface are assembled into large cluster structure, which may diminish the specific surface of P-VO. Therefore, the BET results in Fig. 4(e–f) show that the specific surface area of P-VO nanosheets is 86.58 $m^2\ g^{-1}$, while the T-VO nanobelts display a higher specific surface area of 93.66 $m^2\ g^{-1}$, as shown in Fig. 4(e–f). Besides, element mapping of P-VO in Fig. 3c further indicates the homogeneous distribution of V, O, and N, suggesting the uniform intercalation of PAN. And the good dispersion of V and O also confirms the well combination of T-VO, as the element mapping shown in Fig. 3f. Moreover, TEM images in Fig. 4(a-d) further reveal the flake constructions of P-VO and T-VO with greatly thin thickness.

3.2. Electrochemical performance

To systematically evaluate the electrochemical property enhancement of PAN/THF pillars and mixed V^{4+}/V^{5+} valence in $V_2O_5{\cdot}3H_2O$ composites, the detailed tests were conducted in the potential range of 0.4–1.4 V. Fig. 5a shows the CV curves of P-VO, T-VO, and V_2O_5 at a scan rate of 0.2 mV s^{-1}. Three pairs of redox peaks of P-VO cathode can

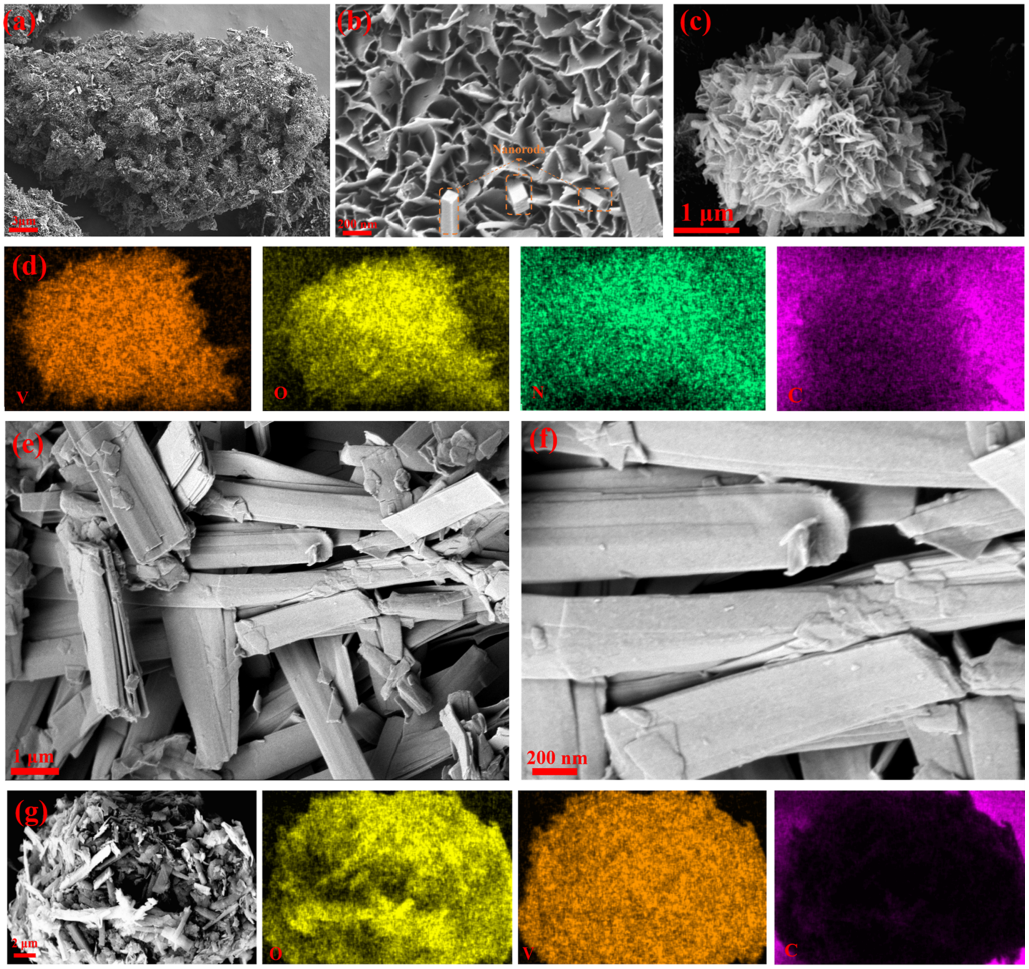

Fig. 3. SEM images of P-VO (a–b) and T-VO (d–e), the corresponding SEM-EDX mapping of V, O, N, and C in P-VO (c), as well as V, O, and C in T-VO (f).

be found at 0.66/0.55 V, 0.81/0.72 V, and 0.99/0.91 V. Meanwhile, three couples of redox peaks of T-VO electrode located at 0.72/0.60 V, 0.97/0.78 V, and 1.07/0.98 V also can be observed. The successive redox peaks of these electrodes indicate the multistep insertion/extraction of Zn^{2+} and the valence variation of vanadium from V^{5+}, V^{4+} to V^{3+} [27,28]. Inversely, the commercial V_2O_5 composite only presents a couple of redox peaks at 1.19/0.95 V. And the peak current densities of P-VO and T-VO are higher than that of commercial V_2O_5, implying their higher electrochemical reactivity induced by mixed V^{4+}/V^{5+} valence [29]. Additionally, the initial charge/discharge (ICD) profiles at 1 A g^{-1} are depicted in Fig. 5b. Both P-VO and T-VO electrodes exhibit sloping discharge plateaus from 0.9 to 0.6 V, while commercial V_2O_5 cathode displays negligible discharge plateaus. This phenomenon further demonstrates the more obvious Zn^{2+} insertion behavior of P-VO and T-VO. The ICD profiles also indicate the much lower initial columbic efficiency (ICE) of commercial V_2O_5 than P-VO and T-VO. Fig. 5(c-d) depict the electrochemical properties of three electrodes at 1 A g^{-1}. Commercial V_2O_5 cathode shows an extremely low initial discharge capacity of 48 mAh g^{-1} and an inferior ICE of 37.5%. It could be attributed to the narrow interlayer of V_2O_5, strong electrostatic interaction and polarization of Zn^{2+}, which will lead to the difficult insertion and severe trap of Zn^{2+}. Inversely, P-VO electrode displays an initial discharge capacity of 200 mAh g^{-1} with a superior ICE of almost 100%, which can gradually increase to 241 mAh g^{-1} after 100 cycles at 1 A g^{-1}. And T-VO cathode shows an initial discharge capacity of 297 mAh g^{-1} with almost 100% ICE, and maintain a capacity retention of 80.1% after 100 cycles. The boosted electrochemical performance is ascribed to the expanded interlayer supported by the organic pillars and the enhanced electrochemical reactivity induced by mixed V^{4+}/V^{5+} dual-valence.

In Fig. 5e, compared with V_2O_5, P-VO cathode furnishes higher average discharge capacities of 278, 264, 243, 227, 202, and 156 mAh g^{-1} at varying current densities of 0.5, 1, 2, 3, 5, and 10 A g^{-1}. And T-VO composite also delivers higher average discharge capacities of 333, 307, 269, 239, 195, and 121 mAh g^{-1} at same current densities. The higher reversible capacity of T-VO at current density below 3 A g^{-1} may be ascribed to its lower charge transfer resistance, faster Zn^{2+} diffusion, and more active sites, which are proved by the following EIS and GITT measures. The Nyquist plots in Fig. 5f show the semicircle diameter of T-VO at high-frequency region is relatively smaller than that of P-VO, implying its lower charge transfer resistance and better electrical conductivity. As shown in Fig. 6, the GITT results show the Zn^{2+} diffusion coefficient of T-VO is larger than that of P-VO, demonstrating the larger transfer rate and smaller energy barrier of Zn^{2+} diffusion. And the D-values of T-VO range from 1.01×10^{-8} to 4.39×10^{-8} cm^{-2} s^{-1} in the discharge process, and 1.04×10^{-8} to 2.72×10^{-8} cm^{-2} s^{-1} in the charge process. However, P-VO delivers the smaller D-values of 1.8×10^{-9} to 6.7×10^{-8} cm^{-2} s^{-1} during the discharge process, and 3.1×10^{-9} to 2.35×10^{-8} cm^{-2} s^{-1} during the charge process. We can observe that the D-values gradually decrease when discharged to 1.4 V, which is related to the constant increasement of Zn^{2+} concentration in lattice of host materials.

The higher electrochemical reactivity, better electrical conductivity, and opener framework are expected to boost the long-term cycling and high-low temperature properties of P-VO and T-VO. As shown in Fig. 7a, the excellent long-term cycling performance of P-VO and T-VO

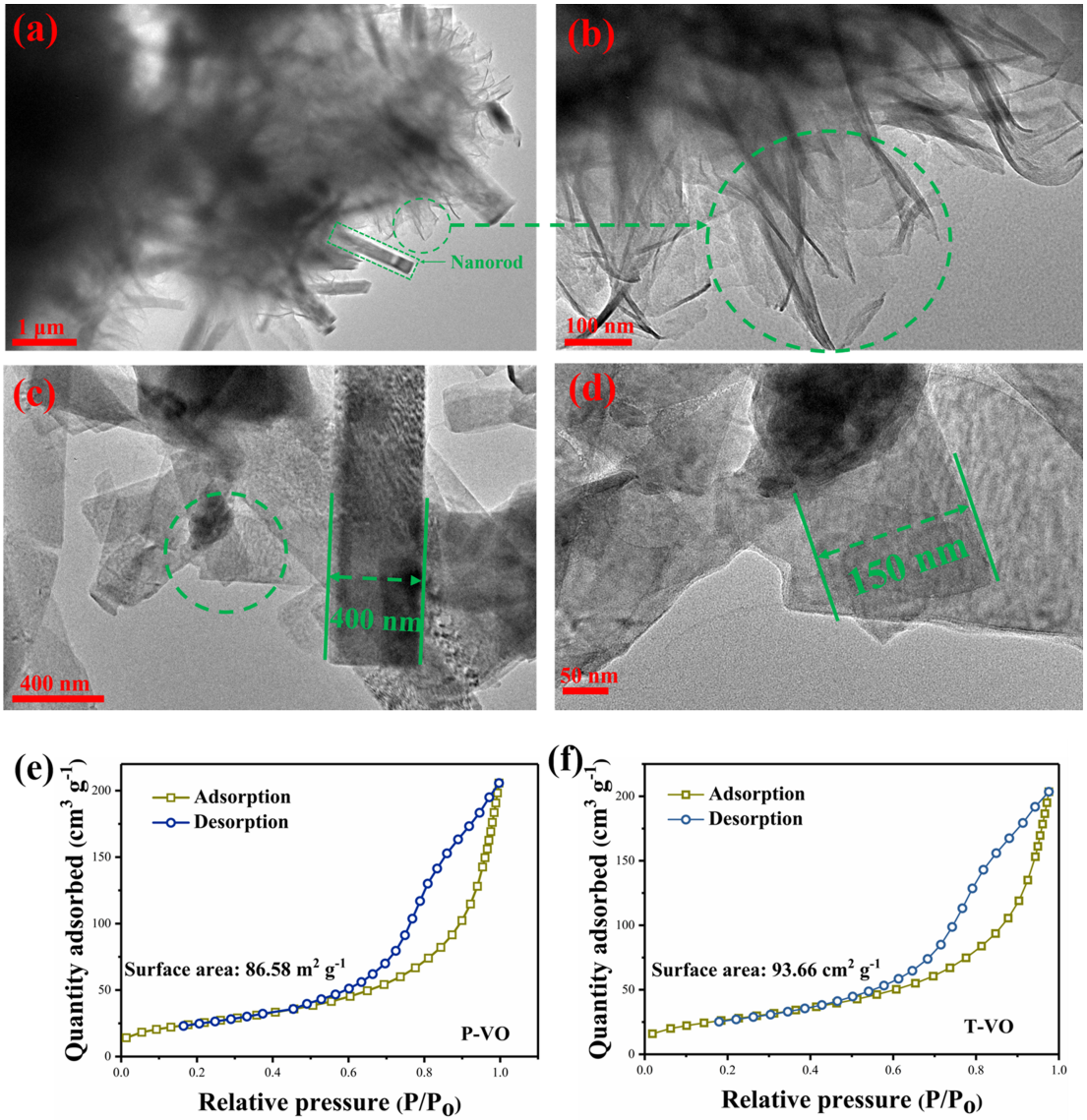

Fig. 4. TEM images of P-VO (a–b) and T-VO (c–d), and Nitrogen adsorption–desorption isotherms (e–f) of P-VO and T-VO.

electrodes can be achieved at higher current densities. When the current density increases to 5 A g^{-1}, P-VO cathode delivers an initial discharge capacity of 217 mAh g^{-1} with a superior coulombic efficiency (CE) of 97.4%. And during the first 200 cycles, the discharge capacity can reach the maximum value of 260 mAh g^{-1}. After 500 cycles, an enduring reversible capacity can be kept at 214 mAh g^{-1}. Notably, after activation at a relatively low current density of 5 A g^{-1}, a reversible discharge capacity of 164 mAh g^{-1} still can be supplied at 10 A g^{-1}, accomplishing a favorite capacity retention of 78.0% after 1000 cycles as shown in Fig. 7b. And T-VO electrode furnishes an initial discharge capacity of 158 mAh g^{-1} with almost 100% CE at 5 A g^{-1}. After the subsequent 500 cycles, the discharge capacity can increase to 195 mAh g^{-1}. And a reversible discharge capacity of 120 mAh g^{-1} can be achieved at 10 A g^{-1} after 1000 cycles with a CE of 83.3%. Different from the contrast at low current density, T-VO electrode supplies lower reversible capacities than P-VO at 5 and 10 A g^{-1}. It may be ascribed to the relatively low mechanical strength of THF pillar and the stronger polarization of Zn^{2+} at larger current densities. Adversely, in virtue of high electrical conductivity, good structural and electrochemical stability [30-33], organic PAN pillar can well maintain better interlayer-expansion effect, thus efficiently withstanding the stronger polarization of Zn^{2+} and supporting the structure of V^{4+}-$V_2O_5{\cdot}3H_2O$. Most importantly, both two composites can sustainably furnish considerable reversible discharge capacities under high and low testing temperatures. As shown in Fig. 7c, with the testing temperature increasing from −15, 0, 15, 30 to 45 °C, P-VO delivers desired discharge capacities of 156, 217, 268, 294, and 281 mAh g^{-1} at 500 mA g^{-1}, T-VO furnishes acceptable discharge capacities of 125, 201, 270, 298, and 273 mAh g^{-1} at 500 mA g^{-1}. The higher discharge capacities of P-VO than those of T-VO at extreme testing temperature of −15 and 45 °C suggest the firmer incorporation of PAN with $V_2O_5{\cdot}3H_2O$, which can endure the repetitive de/intercalation of Zn^{2+}.

In order to explain the high-rate performance of P-VO and T-VO electrodes, multi-scan CV measurement was carried out to reveal the electrochemical kinetics. Fig. 8 (a-b) display the voltammograms of these cathodes from 0.2 to 1.0 mV s^{-1}. It can be observed that the CV curves can preserve similar shapes at each scan rate basically. Meanwhile, the broad reduction and oxidation peaks shift to lower and higher voltages, respectively. The previous literatures reported the currents of reduction peak obey a power-law relationship with scan rates, which is described as $i = av^b$ [34]. And based on the formula of $\log i = b\log v + \log a$, the b-values of P-VO electrode at peak 1, 2, 3, 4, 5 and 6 are computed to be 0.74, 0.98, 0.93, 0.82, 0.98 and 1.00, while the b-values of T-VO cathode are calculated to be 0.90, 0.97, 1.06, 0.95,

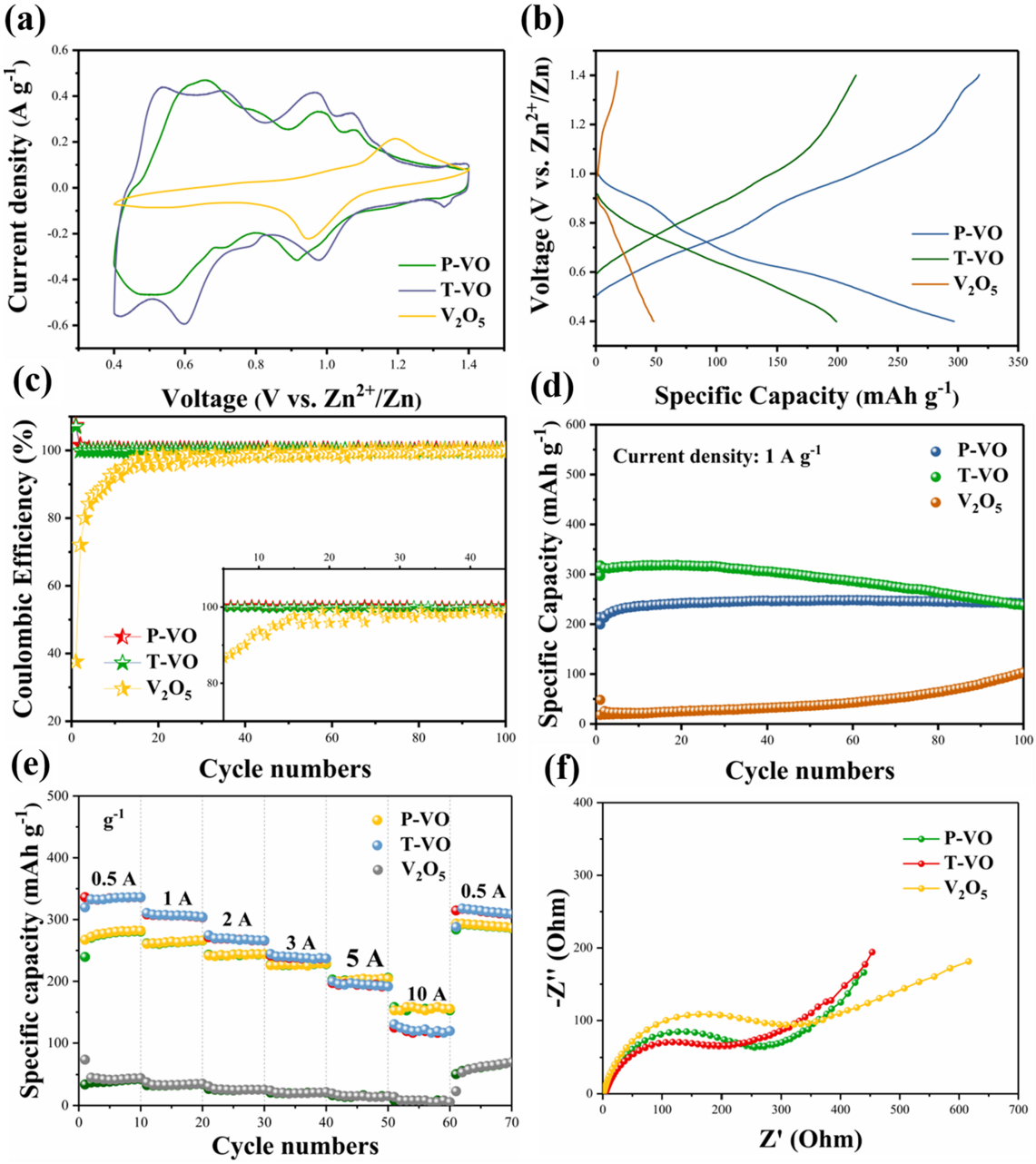

Fig. 5. Electrochemical performance using P-VO, T-VO, and commercial V_2O_5 as cathodes, CV curves (a) at 0.2 mV s^{-1}, initial charging/discharging curves (b), coulombic efficiency (c), cycling performance (d) at 1 A g^{-1}, rate capabilities (e) at various current densities, and Nyquist plots (f) in the frequency range from 100 kHz to 0.01 Hz.

0.90 and 0.96. It is well known that large b-value of 1 implies strong faradic pseudocapacitance behavior [35-37]. Therefore, the capacitive contributions are further quantitatively quantified via separating current response i into surface capacitive effect (k_1v) and diffusion-controlled process ($k_2v^{1/2}$), according to $i = k_1v + k_2v^{1/2}$ [38,39]. As shown in Fig. 8(e–f), with the scan rate rising, the capacitive contribution ratios of P-VO and T-VO cathodes gradually increase from 57.1% to 75.0% and 73.9% to 86.4%, respectively. The different degree of pseudocapacitance behavior may enable two electrodes to deliver discrepant high-rate performance [40].

Furthermore, ex-situ XPS and in-situ XRD measurements were carried out to investigate the storage mechanism of P-VO composite. As shown in Fig. 9a, two peaks can be found at around 1021 and 1045 eV corresponding to Zn $2p_{2/3}$ and Zn $2p_{1/2}$ [20,24,41]. And the intensity of Zn 2p signal increases during discharging process and recovers to initial state during charging process, indicating the good reversibility of Zn^{2+} de/intercalation. The peak of F 1 s at 688 eV also presents intensified trend when discharged to 0.4 V, and still can be detected after charged to 1.4 V, indicating the adsorption of residual $CF_3SO_3^-$ anions on the surface of the electrode. Furthermore, the multi-step V-based redox reaction induced by de/intercalation of Zn^{2+} is also proved. As shown in Fig. 9c, when discharged to 0.7 V, the V^{4+} signal at 515.8 eV gradually intensifies accompanied by a new appearing signal of V^{3+} located at 522.8 eV [42]. And V^{5+} ions are further reduced to V^{4+} and V^{3+} as the discharge depth reaches 0.4 V. After returned to fully charged state, the original V 2p spectrum can be recovered well, revealing the reversible electrochemical reduction of vanadium [43]. In-situ XRD patterns within selected scanning angle domains of 22–37° and 49–54° at first cycle are shown in Fig. 9d. When discharged from pristine state I to fully discharged state II, two characteristic peaks at

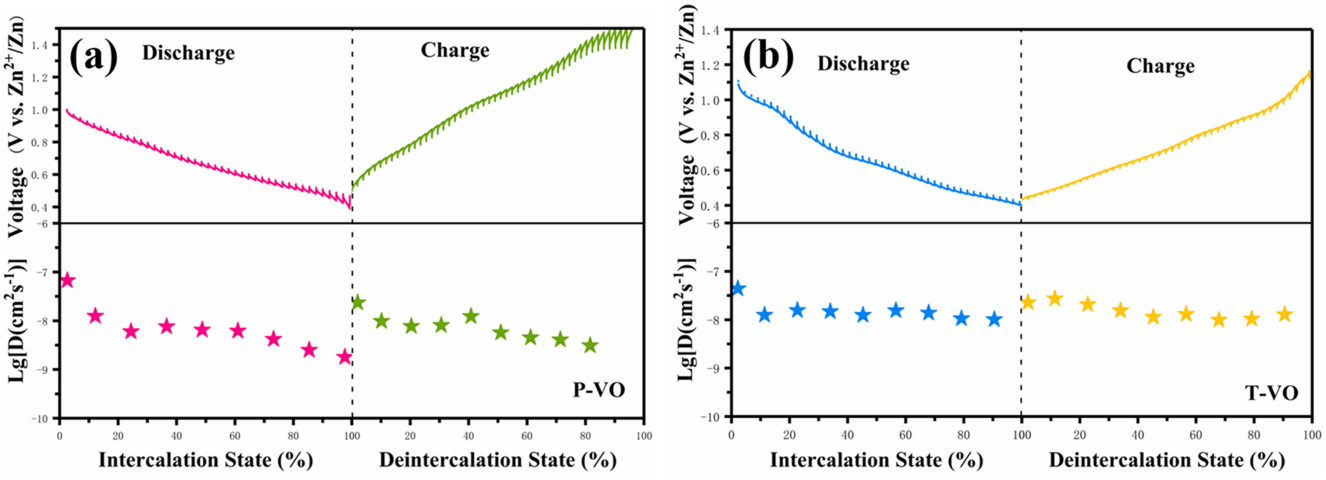

Fig. 6. GITT analysis: the discharge/charge curves and corresponding diffusivity coefficients (D) of Zn^{2+} in discharge and charge processes of P-VO and T-VO.

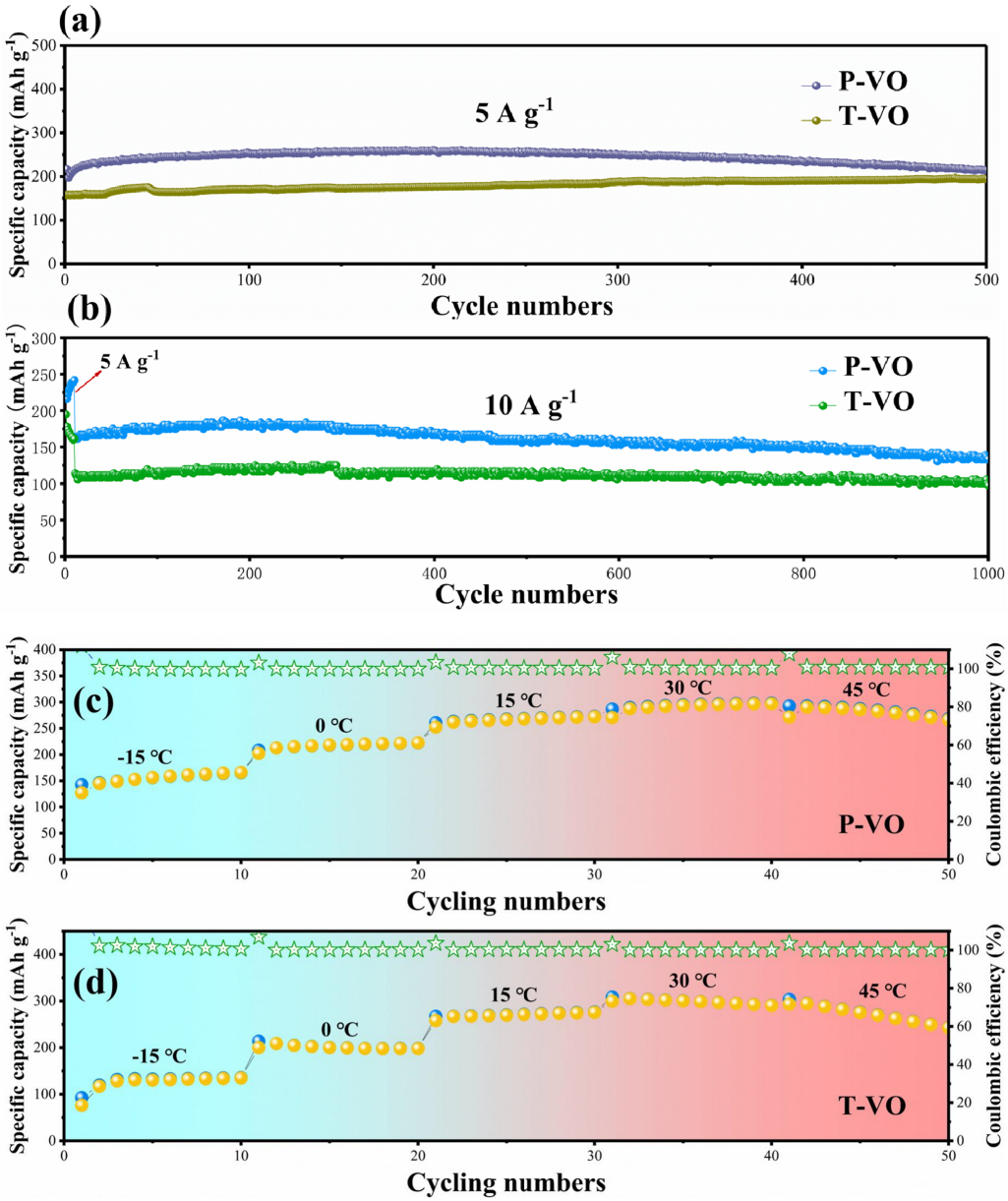

Fig. 7. Electrochemical properties of P-VO and T-VO: long term cycling performance at high current densities of 5 A g^{-1} (a) and 10 A g^{-1} (b), and high-low temperature test (c–d).

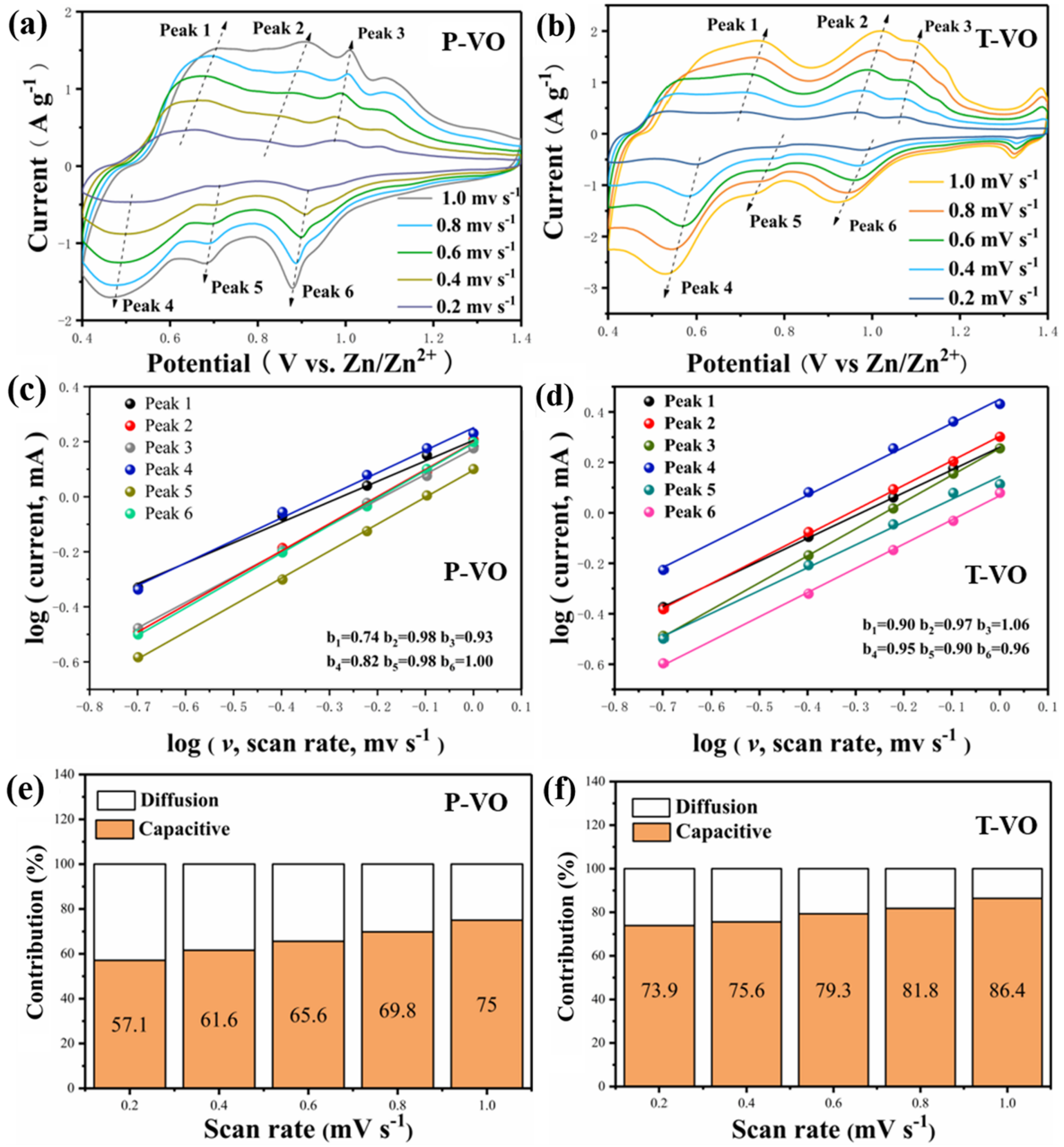

Fig. 8. CV curves at diverse scan rates of 1.0, 0.8, 0.6, 0.4, and 0.2 mV s^{-1}, b-values of $\log i(v) = b\log v + \log a$ at three pairs of redox peaks, and capacitive contribution ratios of P-VO (a, c and e) and T-VO (b, d and f).

25.4° and 50.2° shift toward lower 2θ degrees, and both two peaks return to original position after recovering to fully charged state III, suggesting the reversible expansion/shrink of (500) and (−121) planes induced by de/intercalation of Zn^{2+}. In addition, a new peak with increased intensity appears at 32.9° during discharging process, corresponding to the phase transition from $V_2O_5{\cdot}3H_2O$ to $Zn_xV_2O_5{\cdot}nH_2O$ [44]. And upon charging process, the peak at 32.9° gradually disappears, implying the $Zn_xV_2O_5{\cdot}nH_2O$ phase recovers to $V_2O_5{\cdot}3H_2O$.

4. Summary

PAN and THF pre-intercalated V^{4+}-$V_2O_5{\cdot}3H_2O$ composites were synthesized by organic pillars expansion and V^{4+}/V^{5+} dual-valence regulation strategy. The enlarged interlayer distance and boosted electrochemical reactivity allow P-VO and T-VO to deliver excellent electrochemical performance. Hence, at a current density of 500 mA g^{-1}, P-VO electrode delivers an initial capacity of 251 mAh g^{-1}, while T-VO cathode furnishes a higher initial capacity of 336 mAh g^{-1}. Even the current density rises to 10 A g^{-1}, both P-VO and T-VO composites also present good long-term cycling performance, and keep discharge capacities of 133 mAh g^{-1} and 100 mAh g^{-1} after 1000 cycles, respectively. Additionally, the elevated structural stability allow P-VO and T-VO electrodes to deliver high discharge capacities of 281 mAh g^{-1} and 273 mAh g^{-1} at the highest testing temperature of 45 °C and acceptable discharge capacities of 154 mAh g^{-1} and 125 mAh g^{-1} at the lowest testing temperature of −15 °C.

CRediT authorship contribution statement

Honglin Yan: Methodology; Data analysis; Investigation; Writing-original Draft. **Qiang Ru:** Supervision; Funding Acquisition; Writing-

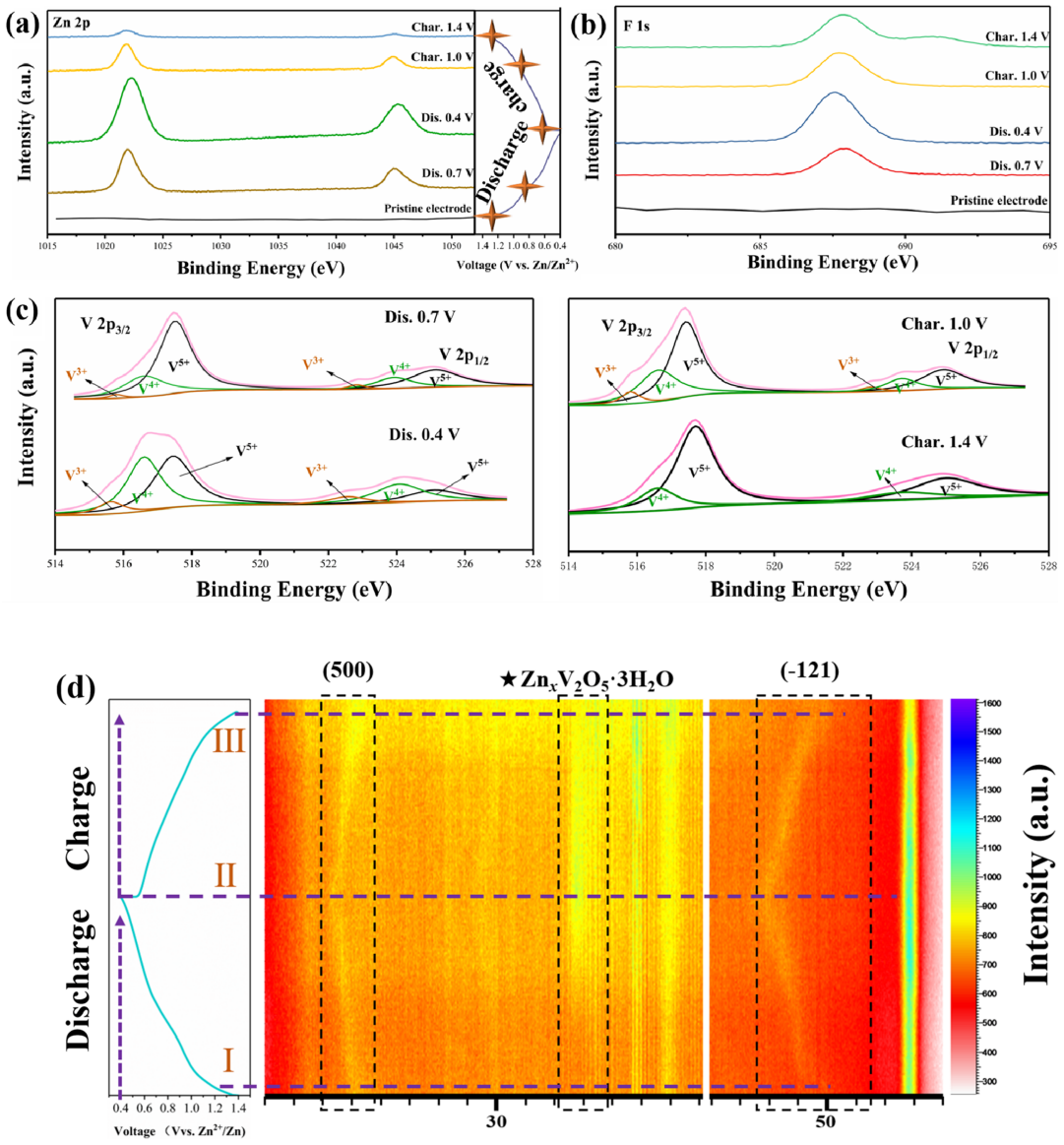

Fig. 9. Ex-situ XPS spectra of Zn 2p (a), F 1s (b), and V 2p (c) at different charge/discharge depths, and in-situ XRD analysis of P-VO electrode (d) at first charging/discharging cycle, state I: pristine electrode, state II: fully discharge, state III: fully charge.

review and Editing. **Ping Gao:** Investigation, Conceptualization, Writing-Reviewing. **Zhenglu Shi:** Software, Writing-Reviewing. **Yuqing Gao:** Investigation, Conceptualization. **Fuming Chen:** Supervision. **Francis Chi-Chun Ling:** Supervision. **Li Wei:** Supervision.

Declaration of Competing Interest

The authors declare that they have no known competing financial interests or personal relationships that could have appeared to influence the work reported in this paper.

Acknowledgements

This work was supported by the union project of National Natural Science Foundation and Guangdong Province (No. U1601214); Special Funds for the Cultivation of Guangdong College Students' Scientific and Technological Innovation (No. pdjha0126); and the Scientific and Technological Plan of Guangzhou City (No. 201804010169), the Department of Education of Guangdong Province (2018KTSCX047) and the Guangdong Basic and Apllied Basic Research Foundation (2019A1515011615).

References

[1] L. Lu, X. Han, J. Li, J. Hua, M. Ouyang, A review on the key issues for lithium-ion battery management in electric vehicles, J. Power Sources 226 (2013) 272–288.
[2] W.-J. Zhang, A review of the electrochemical performance of alloy anodes for li-thium-ion batteries, J. Power Sources 196 (2011) 13–24.
[3] R.K. Guduru, J.C. Icaza, A Brief Review on Multivalent Intercalation Batteries with Aqueous Electrolytes, Nanomaterials 6 (2016) 1–19.
[4] G. Fang, J. Zhou, A. Pan, S. Liang, Recent Advances in Aqueous Zinc-Ion Batteries, ACS Energy Lett. 3 (2018) 2480–2501.
[5] F. Beck, P. Rüetschi, Rechargeable batteries with aqueous electrolytes, Electrochim. Acta 45 (2000) 2467–2482.
[6] H. Wang, R. Tan, Z. Yang, Y. Feng, X. Duan, J. Ma, Stabilization Perspective on Metal Anodes for Aqueous Batteries, Adv. Energy Mater. (2020) 2000962.
[7] M. Song, H. Tan, D. Chao, H.J. Fan, Recent Advances in Zn-Ion Batteries, Adv. Funct. Mater. 28 (2018) 1802564.
[8] B. Tang, L. Shan, S. Liang, J. Zhou, Issues and Opportunities Facing Aqueous Zinc-ion Batteries, Energy Environ. Sci. 12 (2019) 3288–3304.
[9] P. Senguttuvan, S.-D. Han, S. Kim, A.L. Lipson, S. Tepavcevic, T.T. Fister, I.D. Bloom, A.K. Burrell, C.S. Johnson, A High Power Rechargeable Nonaqueous Multivalent Zn/V_2O_5 Battery, Adv. Energy Mater. 6 (2016) 1600826.
[10] L.M. De Juan-Corpuz, R.D. Corpuz, A. Somwangthanaroj, M.T. Nguyen, T. Yonezawa, J. Ma, S. Kheawhom, Binder-Free Centimeter-Long V_2O_5 Nanofibers

on Carbon Cloth as Cathode Material for Zinc-Ion Batteries, Energies 13 (2019) 31.
[11] Y.Q. Yang, Y. Tang, G.Z. Fang, L.T. Shan, J.S. Guo, W.Y. Zhang, C. Wang, L.B. Wang, J. Zhou, S.Q. Liang, Li^+ intercalated V_2O_5 center dot nH_2O with enlarged layer spacing and fast ion diffusion as an aqueous zinc-ion battery cathode, Energy Environ. Sci. 11 (2018) 3157–3162.
[12] C. Xia, J. Guo, P. Li, X. Zhang, H.N. Alshareef, Highly Stable Aqueous Zinc-Ion Storage Using a Layered Calcium Vanadium Oxide Bronze Cathode, Angew. Chem. 57 (2018) 3943–3948.
[13] B.Y. Tang, G.Z. Fang, J. Zhou, L.B. Wang, Y.P. Lei, C. Wang, T.Q. Lin, Y. Tang, S.Q. Liang, Potassium vanadates with stable structure and fast ion diffusion channel as cathode for rechargeable aqueous zinc-ion batteries, Nano Energy 51 (2018) 579–587.
[14] P. He, G. Zhang, X. Liao, M. Yan, X. Xu, Q. An, J. Liu, L. Mai, Sodium Ion Stabilized Vanadium Oxide Nanowire Cathode for High-Performance Zinc-Ion Batteries, Adv. Energy Mater. 8 (2018) 1702463.
[15] L. Shan, Y. Yang, W. Zhang, H. Chen, G. Fang, J. Zhou, S. Liang, Observation of combination displacement/intercalation reaction in aqueous zinc-ion battery, Energy Storage Mater. 18 (2019) 10–14.
[16] F. Ming, H. Liang, Y. Lei, S. Kandambeth, M. Eddaoudi, H.N. Alshareef, Layered $Mg_xV_2O_5{\cdot}nH_2O$ as Cathode Material for High-Performance Aqueous Zinc Ion Batteries, ACS Energy Lett. 3 (2018) 2602–2609.
[17] L. Zhou, Q. Liu, Z. Zhang, K. Zhang, F. Xiong, S. Tan, Q. An, Y.M. Kang, Z. Zhou, L. Mai, Interlayer-Spacing-Regulated $VOPO_4$ Nanosheets with Fast Kinetics for High-Capacity and Durable Rechargeable Magnesium Batteries, Adv. Mater. 30 (2018) 1801984.
[18] L. Peng, Y. Zhu, X. Peng, Z. Fang, W. Chu, Y. Wang, Y. Xie, Y. Li, J.J. Cha, G. Yu, Effective Interlayer Engineering of Two-Dimensional $VOPO_4$ Nanosheets via Controlled Organic Intercalation for Improving Alkali Ion Storage, Nano Lett. 17 (2017) 6273–6279.
[19] J. Huang, Z. Wang, M. Hou, X. Dong, Y. Liu, Y. Wang, Y. Xia, Polyaniline-intercalated manganese dioxide nanolayers as a high-performance cathode material for an aqueous zinc-ion battery, Nat. Commun. 9 (2018) 2906.
[20] F. Liu, Z. Chen, G. Fang, Z. Wang, Y. Cai, B. Tang, J. Zhou, S. Liang, V_2O_5 Nanospheres with Mixed Vanadium Valences as High Electrochemically Active Aqueous Zinc-Ion Battery Cathode, Nano-Micro Letters 11 (2019) 25.
[21] L. Beneš, K. Melánová, J. Svoboda, V. Zima, Intercalation chemistry of layered vanadyl phosphate: a review, J. Incl. Phenom. Macrocycl. Chem. 73 (2012) 33–53.
[22] J. Galy, Vanadium pentoxide and vanadium oxide bronzes—Structural chemistry of single (S) and double (D) layer $M_xV_2O_5$ phases, J. Solid State Chem. 100 (1992) 229–245.
[23] Y. Chen, G. Yang, Z. Zhang, X. Yang, W. Hou, J.J. Zhu, Polyaniline-intercalated layered vanadium oxide nanocomposites–one-pot hydrothermal synthesis and application in lithium battery, Nanoscale 2 (2010) 2131–2138.
[24] V. Soundharrajan, B. Sambandam, S. Kim, M.H. Alfaruqi, D.Y. Putro, J. Jo, S. Kim, V. Mathew, Y.K. Sun, J. Kim, $Na_2V_6O_{16}{\cdot}3H_2O$ Barnesite Nanorod: An Open Door to Display a Stable and High Energy for Aqueous Rechargeable Zn-Ion Batteries as Cathodes, Nano Lett. 18 (2018) 2402–2410.
[25] Q. Pang, C. Sun, Y. Yu, K. Zhao, Z. Zhang, P.M. Voyles, G. Chen, Y. Wei, X. Wang, $H_2V_3O_8$ Nanowire/Graphene Electrodes for Aqueous Rechargeable Zinc Ion Batteries with High Rate Capability and Large Capacity, Adv. Energy Mater. 8 (2018) 1800144.
[26] X.Y. Hu, J. Ouyang, G.C. Liu, M.J. Gao, L.B. Song, J. Zang, W. Chen, Synthesis and Characterization of the Conducting Polymer Micro-Helix Based on the Spirulina Template, Polymers 10 (2018) 882.
[27] C. Liu, Z. Neale, J. Zheng, X. Jia, J. Huang, M. Yan, M. Tian, M. Wang, J. Yang, G. Cao, Expanded hydrated vanadate for high-performance aqueous zinc-ion batteries, Energy Environ. Sci. 12 (2019) 2273–2285.
[28] X. Dai, F. Wan, L. Zhang, H. Cao, Z. Niu, Freestanding graphene/VO_2 composite films for highly stable aqueous Zn-ion batteries with superior rate performance, Energy Storage Mater. 17 (2019) 143–150.
[29] Y. Ding, Y. Peng, W. Chen, Y. Niu, S. Wu, X. Zhang, L. Hu, V-MOF derived porous V_2O_5 nanoplates for high performance aqueous zinc ion battery, Appl. Surf. Sci. 493 (2019) 368–374.
[30] C. Kim, B.Y. Ahn, T.S. Wei, Y. Jo, S. Jeong, Y. Choi, I.D. Kim, J.A. Lewis, High-Power Aqueous Zinc-Ion Batteries for Customized Electronic Devices, ACS Nano (2018) 11838–11846.
[31] F. Wan, L. Zhang, X. Wang, S. Bi, Z. Niu, J. Chen, An Aqueous Rechargeable Zinc-Organic Battery with Hybrid Mechanism, Adv. Funct. Mater. 28 (2018) 1804975.
[32] Y. Luo, R. Guo, T. Li, F. Li, Z. Liu, M. Zheng, B. Wang, Z. Yang, H. Luo, Y. Wan, Application of Polyaniline for Li-Ion Batteries, Lithium-Sulfur Batteries, and Supercapacitors, ChemSusChem 12 (2019) 1591–1611.
[33] S.U. Haque, A. Nasar, M.M.R. Inamuddin, Applications of chitosan (CHI)-reduced graphene oxide (rGO)-polyaniline (PAni) conducting composite electrode for energy generation in glucose biofuel cell, Sci. Rep. 10 (2020) 10428.
[34] H. Li, Q. Yang, F. Mo, G. Liang, Z. Liu, Z. Tang, L. Ma, J. Liu, Z. Shi, C. Zhi, MoS_2 nanosheets with expanded interlayer spacing for rechargeable aqueous Zn-ion batteries, Energy Storage Mater. 19 (2019) 94–101.
[35] T. Jiao, Q. Yang, S. Wu, Z. Wang, D. Chen, D. Shen, B. Liu, J. Cheng, H. Li, L. Ma, C. Zhi, W. Zhang, Binder-free hierarchical VS_2 electrodes for high-performance aqueous Zn ion batteries towards commercial level mass loading, J. Mater. Chem. A 7 (2019) 16330–16338.
[36] Y. Li, Z. Huang, P.K. Kalambate, Y. Zhong, Z. Huang, M. Xie, Y. Shen, Y. Huang, V_2O_5 nanopaper as a cathode material with high capacity and long cycle life for rechargeable aqueous zinc-ion battery, Nano Energy 60 (2019) 752–759.
[37] X. Wang, S. Zheng, F. Zhou, J. Qin, X. Shi, S. Wang, C. Sun, X. Bao, Z.S. Wu, Scalable fabrication of printed Zn//MnO_2 planar micro-batteries with high volumetric energy density and exceptional safety, Natl. Sci. Rev. 7 (2020) 64–72.
[38] M. Sun, D.S. Li, Y.F. Wang, W.L. Liu, M.M. Ren, F.G. Kong, S.J. Wang, Y.Z. Guo, Y.M. Liu, Mn_3O_4@NC Composite Nanorods as a Cathode for Rechargeable Aqueous Zn-Ion Batteries, ChemElectroChem 6 (2019) 2510–2516.
[39] B.T. Liu, X.M. Shi, X.Y. Lang, L. Gu, Z. Wen, M. Zhao, Q. Jiang, Extraordinary pseudocapacitive energy storage triggered by phase transformation in hierarchical vanadium oxides, Nat. Commun. 9 (2018) 1375.
[40] C. Xia, J. Guo, Y. Lei, H. Liang, C. Zhao, H.N. Alshareef, Rechargeable Aqueous Zinc-Ion Battery Based on Porous Framework Zinc Pyrovanadate Intercalation Cathode, Adv. Mater. 30 (2018) 1705580.
[41] X. Wang, Y. Li, S. Wang, F. Zhou, P. Das, C. Sun, S. Zheng, Z.S. Wu, 2D Amorphous V_2O_5/Graphene Heterostructures for High-Safety Aqueous Zn-Ion Batteries with Unprecedented Capacity and Ultrahigh Rate Capability, Adv. Energy Mater. 10 (2020) 2000081.
[42] N. Zhang, M. Jia, Y. Dong, Y. Wang, J. Xu, Y. Liu, L. Jiao, F. Cheng, Hydrated Layered Vanadium Oxide as a Highly Reversible Cathode for Rechargeable Aqueous Zinc Batteries, Adv. Funct. Mater. 29 (2019) 1807331.
[43] D. Kundu, B.D. Adams, V. Duffort, S.H. Vajargah, L.F. Nazar, A high-capacity and long-life aqueous rechargeable zinc battery using a metal oxide intercalation cathode, Nat. Energy 1 (2016) 16119.
[44] N. Zhang, Y. Dong, M. Jia, X. Bian, Y. Wang, M. Qiu, J. Xu, Y. Liu, L. Jiao, F. Cheng, Rechargeable Aqueous Zn–V_2O_5 Battery with High Energy Density and Long Cycle Life, ACS Energy Lett. 3 (2018) 1366–1372.